JACS
JOURNAL OF THE AMERICAN CHEMICAL SOCIETY
Article
pubs.acs.org/JACS

Melting of Pb Charge Glass and Simultaneous Pb−Cr Charge Transfer in $PbCrO_3$ as the Origin of Volume Collapse

Runze Yu,[*,†,■] Hajime Hojo,[†] Tetsu Watanuki,[‡] Masaichiro Mizumaki,[§] Takashi Mizokawa,[∥,○] Kengo Oka,[†,▲] Hyunjeong Kim,[⊥] Akihiko Machida,[‡] Kouji Sakaki,[⊥] Yumiko Nakamura,[⊥] Akane Agui,[‡] Daisuke Mori,[#] Yoshiyuki Inaguma,[#] Martin Schlipf,[▽,●] Konstantin Z. Rushchanskii,[▽] Marjana Ležaić,[▽] Masaaki Matsuda,[□] Jie Ma,[□] Stuart Calder,[□] Masahiko Isobe,[⊗,△] Yuichi Ikuhara,[¶] and Masaki Azuma[*,†]

[†]Materials and Structures Laboratory, Tokyo Institute of Technology, 4259 Nagatsuta, Midori, Yokohama, 226-8503, Japan
[‡]Quantum Beam Science Center, Japan Atomic Energy Agency, Sayo, Hyogo 679-5148, Japan
[§]Japan Synchrotron Radiation Research Institute, Sayo, Hyogo 679-5198, Japan
[∥]Department of Complexity Science and Engineering, University of Tokyo, Kashiwa, Chiba 277-8561, Japan
[⊥]National Institute of Advanced Industrial Science and Technology, Central 5, 1-1-1 Higashi, Tsukuba, Ibaraki 305-8565, Japan
[#]Department of Chemistry, Faculty of Science, Gakushuin University, 1-5-1 Mejiro, Toshima, Tokyo 171-8588, Japan
[▽]Peter Grünberg Institut, Forschungszentrum Jülich and JARA, Jülich 52425, Germany
[□]Quantum Condensed Matter Division, Oak Ridge National Laboratory, Oak Ridge, Tennessee 37831, United States
[⊗]Institute for Solid State Physics, University of Tokyo, Chiba 277-8581, Japan
[¶]Institute of Engineering Innovation, University of Tokyo, Bunkyo, Tokyo 113-8656, Japan

Supporting Information

ABSTRACT: A metal to insulator transition in integer or half integer charge systems can be regarded as crystallization of charges. The insulating state tends to have a glassy nature when randomness or geometrical frustration exists. We report that the charge glass state is realized in a perovskite compound $PbCrO_3$, which has been known for almost 50 years, without any obvious inhomogeneity or triangular arrangement in the charge system. $PbCrO_3$ has a valence state of $Pb^{2+}{}_{0.5}Pb^{4+}{}_{0.5}Cr^{3+}O_3$ with Pb^{2+}−Pb^{4+} correlation length of three lattice-spacings at ambient condition. A pressure induced melting of charge glass and simultaneous Pb−Cr charge transfer causes an insulator to metal transition and ∼10% volume collapse.

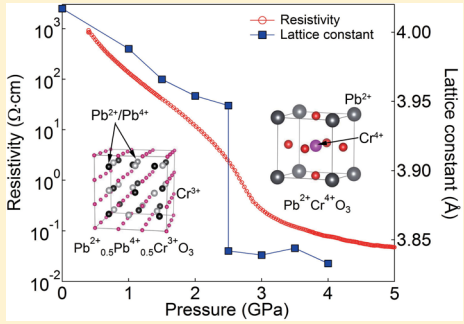

1. INTRODUCTION

Charge degrees of freedom of transition metal ions give rise to various fascinating properties of transition-metal compounds, such as superconductivity or magnetoresistance. The ordering or disproportionation of charges in systems with integer or half integer charge number per atom, such as $Pr_{0.5}Ca_{0.5}MnO_3$[1] or $CaFeO_3$,[2] causes metal−insulator transitions. These can be regarded as crystallization of charges. The insulating state tends to have a glassy nature when randomly located dopants are introduced.[3] A charge cluster glass state owing to geometric frustration arising from a triangular arrangement without randomness was recently found in an organic compound θ-$(BEDT\text{-}TTF)_2RbZn(SCN)_4$ and is attracting significant attention.[4]

Bi and Pb are main group elements, but they have a charge degree of freedom depending on $6s^0$ and $6s^2$ electronic configurations. These are so-called valence skippers because the $6s^1$ state is prohibited.[5] This characteristic of Pb is utilized for lead-acid batteries.[6] Charge disproportionation of Bi is found in perovskites $Ba^{2+}Bi^{3+}{}_{0.5}Bi^{5+}{}_{0.5}O_3$[7] and $Bi^{3+}{}_{0.5}Bi^{5+}{}_{0.5}Ni^{2+}O_3$.[8] The latter compound exhibits a pressure induced intermetallic charge transfer between Bi^{5+} and Ni^{2+} leading to volume collapse and insulator to metal transition.[9,10] Similar intermetallic charge transfers were observed in $FeTiO_3$,[11] hexagonal Bi/Ir perovskite[12] and double perovskite $LaCu_3Fe_4O_{12}$.[13] $PbCrO_3$ has long been regarded as a perovskite compound with a $Pb^{2+}Cr^{4+}O_3$ oxidation state like $CaCrO_3$ and $SrCrO_3$.[14−16] The latter two compounds are extensively studied as rare examples of antiferromagnetic metals with complex orbital ordering and a *C*-type spin structure.[17−20] Despite the fact that Sr^{2+} and Pb^{2+} have similar ionic radii and that $PbCrO_3$ and $SrCrO_3$ have the same cubic structure with $Pm\bar{3}m$ symmetry, $PbCrO_3$ is an antiferromagnetic insulator with an enhanced lattice constant of 4.01 Å, namely, 4.8% larger than that of $SrCrO_3$.[14,21,22] This value is even larger than that of

Received: August 12, 2015
Published: September 15, 2015

DOI: 10.1021/jacs.5b08216
J. Am. Chem. Soc. 2015, 137, 12719−12728

$LaCrO_3$ where Cr is 3+. These facts strongly suggest that the electronic states of the chromium ions in $PbCrO_3$ and $SrCrO_3$ are different. Recently, $PbCrO_3$ was reported to exhibit a large pressure-induced volume collapse of 9.8%[22] at 1.6 GPa accompanied by a change in the slope of pressure dependence of resistivity.[23] A scenario based on a first-principles calculation indicating a tetragonal to cubic transition in $PbCrO_3$ was proposed by Ganesh and Cohen as the origin of this volume collapse,[24] but such a tetragonal distortion in $PbCrO_3$ has never been observed. Moreover, to our knowledge, only two first-principles calculations so far have reproduced the experimentally observed insulating nature of $PbCrO_3$, one of them assuming a Pb−Cr antisite disorder[25] (that, however, still underestimates the volume) and the other assuming a charge-disproportionated Cr site.[26] The latter calculation reveals a minimum in the total energy close to the energy of the cubic phase, but corresponding to the experimentally observed volume. From a structural point of view, X-ray and neutron diffraction Bragg peaks attained for $PbCrO_3$ are broad, suggesting the presence of some kind of defect structure. Indeed, a modulated microdomain structure was observed by Arévalo-López and Alario-Franco in high-resolution transmission electron microscopy (HRTEM)[27] and was attributed to the periodical distribution of lead deficiency. However, it does not explain the insulating nature of $PbCrO_3$, its large lattice constant, and the pressure-induced volume collapse. Here, we investigate the structure and electronic configuration of $PbCrO_3$ employing synchrotron X-ray powder diffraction (SXRD), pair distribution function (PDF) analysis, neutron powder diffraction, scanning TEM (STEM), X-ray photoelectron spectroscopy (XPS), density functional theory (DFT) calculation and X-ray absorption spectroscopy (XAS). We show that $PbCrO_3$ has a $Pb^{2+}_{0.5}Pb^{4+}_{0.5}Cr^{3+}O_3$ valence state with glassy distribution of Pb^{2+} and Pb^{4+} ions and that intermetallic charge transfer between Pb^{4+} and Cr^{3+} induced by application of pressure or Sr substitution for Pb leads to the volume collapse and insulator to metal transition.

2. METHODS SECTION

Polycrystalline samples were prepared from a mixture of PbO and CrO_2 at a ratio of 1.1:1 and from PbO, PbO_2, SrO, and Cr_2O_3 with stoichiometric compositions for $PbCrO_3$ and for $Pb_{1-x}Sr_xCrO_3$, respectively. These mixtures were sealed into gold capsules with a diameter of 3.6 mm and a height of 5 mm and were treated at 8 GPa and 1073 K for 30 min in a cubic-anvil-type high-pressure apparatus. The obtained $PbCrO_3$ sample was crushed into powder and washed with dilute HCl acid to remove the remaining PbO and other impurities. The $SrCrO_3$ was prepared in the same way as reported.[18] SXRD data for $PbCrO_3$ and $Pb_{1-x}Sr_xCrO_3$ at ambient pressure were collected on a large Debye−Scherrer camera installed on the BL02B2 beamline (with a wavelength of 0.420002 Å) of SPring-8. The energy-dispersive SXRD data for $PbCrO_3$ at high pressure were collected at beamline BL14B1of SPring-8 using a cubic-anvil-type high-pressure apparatus with a solid-state detector fixed at $2\theta = 4.0°$. The chemical composition of $PbCrO_3$ was determined by ICP spectrometry with a HORIBA Ultima 2 ICP optical emission spectrometer. HRTEM and STEM observations were carried out using JEOL JEM-2100F transmission electron microscope and ARM-200F scanning transmission electron microscope with high-angel anular dark-field (HAADF) detector, respectively. The temperature dependence of the magnetic susceptibility of $PbCrO_3$ was measured with a SQUID magnetometer (Quantum Design, MPMS XL) in an external magnetic field of 10 kOe. Electrical resistivity under high-pressure and high temperature conditions was measured with a cubic anvil-type high-pressure apparatus by a four-probe method. Gold electrodes were deposited on both faces of a disk-shaped sample (φ4 mm × 1.7 mm). The pressure medium was pyrophyllite. The resistivity of $Pb_{1-x}Sr_xCrO_3$ at room temperature was measured by a two-probe method.

PDF data were collected by using the diffractometer[28] at beamline BL22XU of SPring-8. A powder sample of $PbCrO_3$ was loaded into a cylindrical kapton capillary of 1 mm in diameter. Monochromatized synchrotron X-ray of 69.91 keV (λ = 0.1773 Å) was irradiated to the sample at room temperature. The total scattering data that includes both Bragg reflection and diffuse scattering was recorded on a large flat-type imaging plate detector with the area size of 400 × 400 mm^2. The sample capillary was rotated around the cylindrical axis during the measurement in order to make further improvements of both the absorption correction and the powder average. The scattering data was obtained up to the maximum momentum transfer Q_{max} of 27 $Å^{-1}$ ($2\theta_{max}$ = 45 deg.). The scattering signal from the kapton capillary was removed by subtraction of the empty capillary data. Various other corrections were made as shown in the reference.[29] The PDF was obtained by using the PDFgetX2 program.[30] The local structural analysis was made by using the PDFgui program.[31]

The valence states of $PbCrO_3$ were determined by XPS. The Pb-4f and Bi-4f XPS measurements were performed at 300 K with E = 7935 and 5950 eV at the undulator beamlines BL47XU and BL15XU of SPring-8, respectively. The Cr-2p XPS measurement was performed at 300 K with E = 1253.6 eV (Mg Kα source). For these measurements, hemispherical photoelectron analyzers (SES2002/R-4000 and JPS9200) were used. The polycrystalline samples were fractured in situ for the XPS measurements. The binding energies were calibrated using Au-$4f_{7/2}$ peak (84.0 eV) and Fermi edge of gold reference samples. The total-energy resolutions were 280 meV at E = 7935 eV, 230 meV at E = 5950 eV and 1 eV at E = 1253.6 eV. The Cr-2p XPS spectrum is analyzed by the standard configuration-interaction calculation on the CrO_6 cluster model for $LaCr^{3+}O_3$.[32] Neutron powder diffraction data was collected at beamline HB-2A at HFIR, ORNL on a sample without acid washing loaded into a vanadium can. Using a Ge monochromator measurements were performed with wavelengths of 2.41 Å. Polarized neutron diffraction data was collected at beamline HB-1 at HFIR, ORNL, using neutron beam with wavelength of 2.46 Å polarized by Heusler monochromator. XAS spectra around the O K-edge for the $Pb_{1-x}Sr_xCrO_3$ sample were measured at 300 K by a total-electron-yield method at BL27SU of SPring-8. Energy resolution ($E/\Delta E$) at the O K-edge was greater than 5000. The incident photon energy was calibrated by measuring the energies of the Ti $L_{2,3}$-edges of TiO_2 and the Ni $L_{2,3}$-edges of NiO. Each powder sample was pasted uniformly on a sample holder by using carbon tape.

We carried out first-principles density-functional calculations within the spin-polarized generalized gradient approximation (GGA). Both PBE[33] and PBEsol[34] functionals yield the same ground state (the energies indicated in the text are obtained with PBEsol). Correlation effects at the Cr site were taken into account within the DFT+U approach of Liechtenstein et al.,[35] with U = 4 eV and J = 1 eV. For all crystal symmetries, we performed a full relaxation of the G-type antiferromagnetic unit cell, employing the Vienna ab initio simulation package (VASP)[36] with the PAW potentials[37] up to an accuracy of 0.005 eV/Å with a plane-wave cutoff of 500 eV and a k-point mesh corresponding to 8 × 8 × 8 in the simple perovskite unit cell. Spin−orbit interaction was included. The genetic algorithm based calculations were performed with the USPEX code.[38−40] For the 40-atoms unit cell with variable lattice vectors, we ran 30 generations with about 30 individuals in each (i.e., in total, about 1000 structures were considered).

3. RESULTS AND DISCUSSION

Since Arévalo-López's HRTEM study was performed on a sample with considerable amounts of impurity phases and the chemical analysis of the composition was absent, we started with the preparation of a sample without detectable secondary phase. The SXRD pattern of our $PbCrO_3$ powder is shown in

DOI: 10.1021/jacs.5b08216
J. Am. Chem. Soc. 2015, 137, 12719−12728

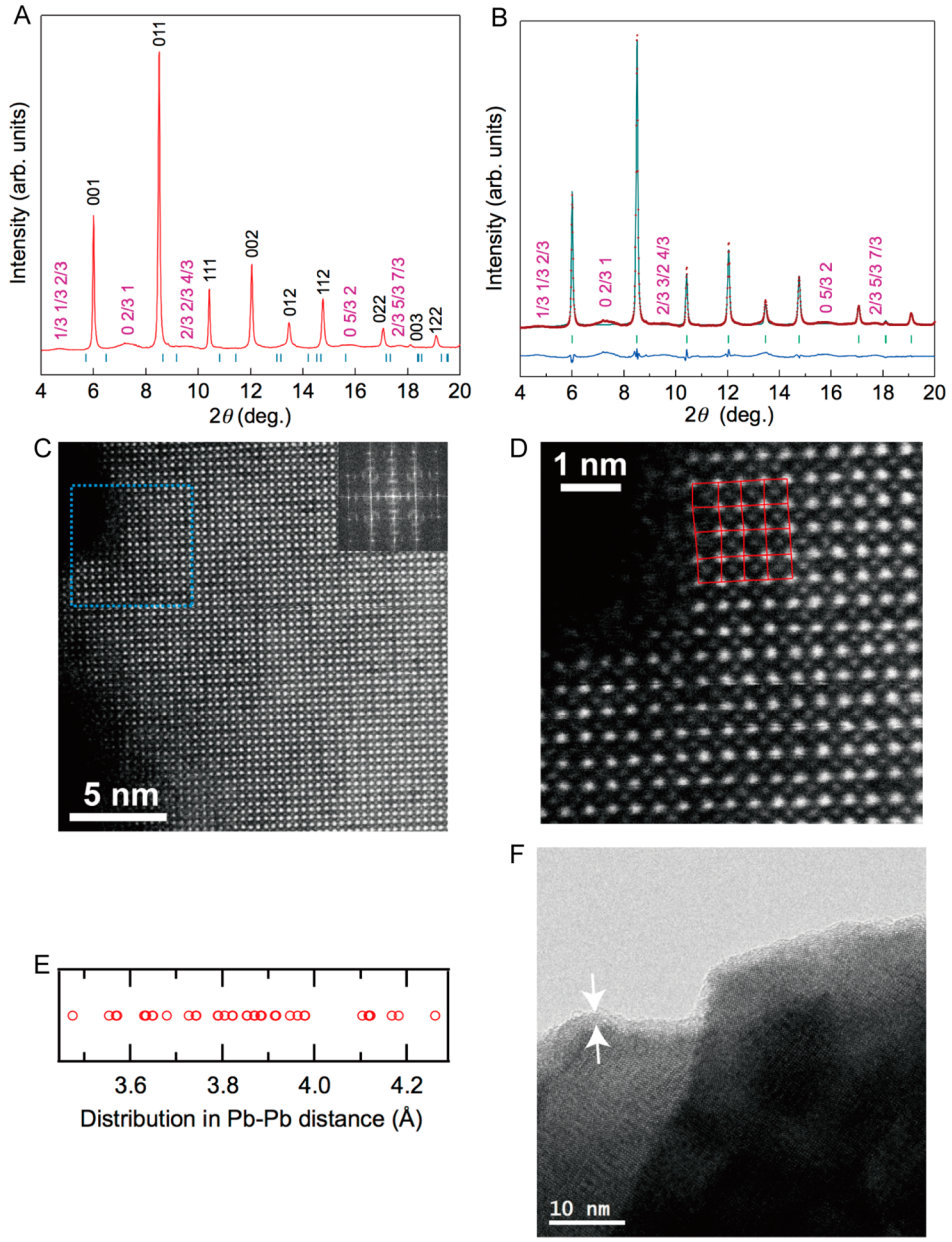

Figure 1. Structural data for $PbCrO_3$ indicating the presence of modulated structure. (A) SXRD pattern of $PbCrO_3$. The pink labels denote the diffuse scattering that reflect the modulated structure. The blue lines denote the Bragg reflection positions expected for the tetragonal structure with c/a = 0.88 proposed by Ganesh and Cohen.[24] (B) Rietveld refinement of SXRD pattern of $PbCrO_3$ at room temperature. Observed (+), calculated (line), and their difference (bottom line) profiles are shown. The pink labels denote the diffuse scattering that reflect the modulated structure. The blue lines denote the Bragg reflection positions. (C) HAADF STEM image viewed along the perovskite [001] zone axis. Inset shows the FFT pattern of this image. (D) Magnified HAADF STEM image of the dotted region in (C). The location of Pb columns are connected with red lines at thin edge part of the sample. (E) The distribution of Pb−Pb distances measured in (D). (F) HRTEM image with lower magnification. The arrows mark the amorphous layer.

Figure 1A. All the peaks can be indexed for a cubic unit cell with $a = 4.0028 \pm 0.0076$ Å. Contrary to previous studies,[27] no additional peak from any impurity phase was found. The broad features at around 5° and 7° do not come from an impurity phase; in fact, they are 1/3 1/3 2/3 and 0 2/3 1 (See the indices in Figure 1A) diffuse scatterings that reflect the modulated structure observed by HRTEM.[27] The peak positions expected for the tetragonal structure with $c/a = 0.88$ proposed by Ganesh and Cohen[24] are indicated in the Figure 1A as the blue marks at the bottom. The peaks are broad, but no peak splitting indicating such tetragonal distortion was found. Furthermore, if the tetragonal distortion is the origin of the peak broadening, the width of *hk*0 and 00*l* peaks should be smaller than *hkl* peaks. However, such difference was not observed, the full width at half-maximum (FWHM) of all peaks were 0.1°. The Rietveld refinement assuming a cubic perovskite structure (see Figure 1B and Table S1) resulted in an unusualy large atomic displacement factor B_{iso} of Pb 6.31 Å^2 (corresponding to $U_{iso} = 0.080$ Å^2) for Pb, suggesting the presence of structural disorder, either of Pb deficiency or splitting of the Pb position.

The cation ratio of the pure-$PbCrO_3$ sample as determined by inductively coupled plasma (ICP) was Pb: Cr = 1.01 ± 0.02. This value is inconsistent with Arévalo-López's report[27] that

DOI: 10.1021/jacs.5b08216
J. Am. Chem. Soc. 2015, 137, 12719−12728

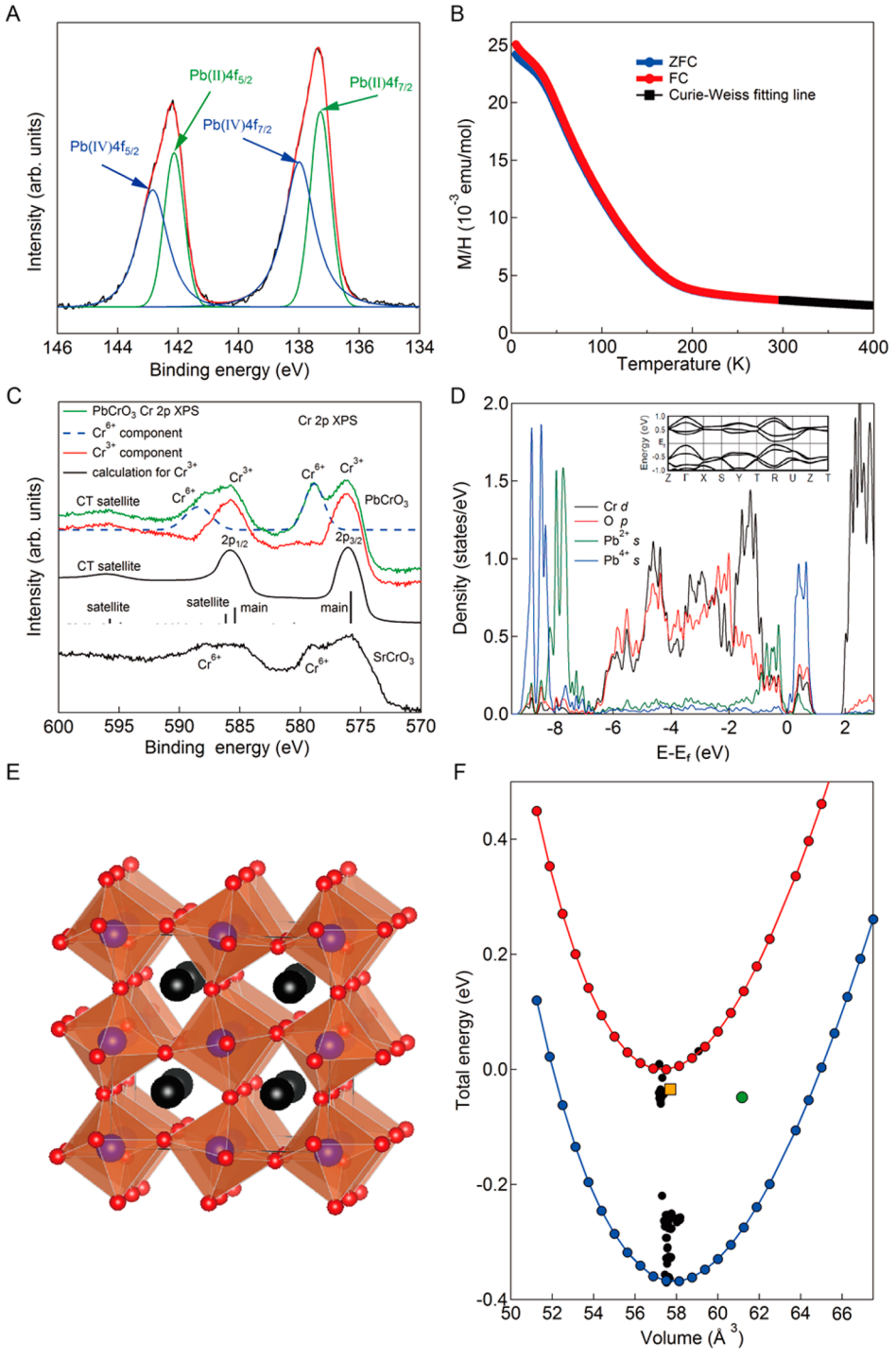

Figure 2. Investigations of the valences of Pb and Cr ions revealing $Pb^{2+}_{0.5}Pb^{4+}_{0.5}Cr^{3+}O_3$ valence state. (A) Pb-4f core-level XPS spectrum of $PbCrO_3$ with the fitting results. The black and red lines are observed spectra and total fitted spectrum, respectively; the green and blue lines show the contributions of Pb^{2+} and Pb^{4+}, respectively. (B) Temperature dependence of magnetic susceptibility of pure $PbCrO_3$ and the fitting results to the Curie–Weiss law. (C) Cr-2p core-level XPS spectra of pure $PbCrO_3$ sample compared with that of $SrCrO_3$. The charge-transfer (CT) satellite is clearly observed in $PbCrO_3$ which is similar to $LaCr^{3+}O_3$ and is different from $SrCr^{4+}O_3$. After subtraction of the Cr^{6+} component from the surface layer (dashed line), the XPS spectrum is compared with the cluster model calculation for Cr^{3+} oxides. (D) Atom and orbital-decomposed DOS calculated for the Pb^{2+}/Pb^{4+} ordered structure (space group *Pmnm*) with $U = 4$ eV, $J = 1$ eV on Cr d-states. The zero of the abscissa corresponds to the Fermi energy E_F. The 4+ valence of one of the Pb ions is reflected in its high s-DOS just above E_F. (E) The Pb^{2+}/Pb^{4+} ordered crystal structure (space group *Pmnm*). The black and blue atoms are Pb and Cr, respectively. (F) Total energy per formula unit vs volume of the antiferromagnetic simple cubic (red circles) and the Pb^{2+}/Pb^{4+} ordered structure (blue circles); the lines of the corresponding colors are the fits to the Murnaghan equation of state.[46] A tetragonal state with *P4mm* symmetry (orange square) and a Cr-charge-disproportionated state (large green circle) are shown for comparison (both at their optimized volumes). The black circles indicate various metastable structures found by the genetic algorithm-based search for the ground state. All calculations are performed with $U = 4$ eV and $J = 1$ eV on Cr d-states.

DOI: 10.1021/jacs.5b08216
J. Am. Chem. Soc. 2015, 137, 12719–12728

10% of the lead deficiency is the origin of the modulated structure observed by HRTEM. HAADF STEM image and the fast Fourier transform (FFT) of this image for our $PbCrO_3$ sample viewed along the perovskite [001] zone axis are shown in Figure 1C and the inset of Figure 1C. Bright spots corresponds to the Pb column locations while Cr columns surrounded by four Pb columns appear as darker spots. The FFT pattern shows diffuse intensity in the form of streaks, which is characteristic of modulated structures arising from periodic perturbations or modulations of the basic cell with a peridicity of $\sim 3a_0$ where a_0 is the lattice parameter of the cubic cell. The FFT pattern are similar to those in the previous report.[27] These results clearly indicate that the modulated structure is not caused by lead deficiency. The lateral shift of Pb positions is evident in the magnified HAADF image shown in Figure 1D taken at the thin edge of a grain where the effect of lateral modulation within each column is minimized. To quantitatively evaluate the shift, the location of Pb ions are connected with red lines and the distribution of Pb−Pb distances are plotted in Figure 1E. The Pb−Pb distances range from ∼3.5 to ∼4.3 Å. As shown below, this modulation should be attributed to partial ordering of Pb^{2+} and Pb^{4+}. High-resulution TEM (HRTEM) image with lower magnification (Figure 1F) shows the presence of amorphous phase at the surface of grains. However, consideing the thickness of the amorphous region of ∼2 nm, only 0.01 of the typical grain size, and the local EDX result of unity ratio of Pb/Cr, our ICP result is not affected. As discussed later, we tentatively assign this to amorphous $PbCrO_4$.

Next, hard X-ray photoelectron spectroscopy was conducted to investigate the valence state of lead. The Pb-4f Hard X-ray photoemission (HAXPES) spectrum for $PbCrO_3$ is shown in Figure 2A. Both the $4f_{5/2}$ and $4f_{7/2}$ peaks that are split by the spin−orbit interaction are doublet, asymmetric with shoulders at higher binding energy, suggesting the coexistence of two valence states, namely, Pb^{2+} and Pb^{4+}. The blue and green lines for both the $4f_{5/2}$ and $4f_{7/2}$ peaks show the fitting results, under the assumption of the presence of two individual peaks with fitting parameters summarized in Table S2. The ratios between the peak areas of Pb $4f_{7/2}$ and Pb $4f_{5/2}$ for both Pb^{2+} and Pb^{4+} are close to the theoretical value of 4:3.[41] It should also be noted that the splitting of Pb^{2+} and Pb^{4+}, 0.75 eV, agrees well with the value we obtained from first-principles calculations (0.68−1 eV) assuming the Pb^{2+}/Pb^{4+} ordering as discussed later. Furthermore, similar asymmetric HAXPES spectrum as shown in Figure S1 with shoulders at higher binding energy was observed for $BiNiO_3$ where Bi^{3+}/Bi^{5+} disproportionation was established[8] (fitting parameters were summarized in Table S3). The $Pb^{2+}{}_{0.5}Pb^{4+}{}_{0.5}$ valence state of Pb is therefore confirmed.

Since Pb is disproportionated into Pb^{2+} and Pb^{4+}, the valence of the Cr ion should be 3+. This explains the large lattice constant of $PbCrO_3$. The bond valence sum[42] for chromium ions calculated from the Cr−O bond length of 2.0014 Å, namely, half of the *a*-axis length, is +2.85, which is close to +3. The temperature dependence of the magnetic susceptibility of $PbCrO_3$ measured on heating after zero-field cooling (ZFC) and on cooling in a magnetic field (FC) from 5 to 400 K is shown in Figure 2B. The data between 300 and 400 K, well above the Neel temperature of 240 K[14] were fitted to the Curie−Weiss law with a temperature-independent term, $\chi = \chi_0 + C/(T - \theta)$, where χ_0 is temperature-independent susceptibility, C is the Curie constant, and θ is the Weiss temperature. The fitting result shown as a black line in Figure 2B gives $\chi_0 = -3.4 \times 10^{-4}$ emu/mol, $C = 1.72$ emu/mol·K, and $\theta = -283$ K indicating that the effective magnetic moment is 3.71 μ_B, which is close to 3.87 μ_B expected for Cr^{3+}, rather than 2.82 μ_B for Cr^{4+}.

The trivalent nature of the Cr ion was further confirmed by binding energy and charge-transfer (CT) satellites in Cr-2p XPS as shown in Figure 2C. The Cr-2p XPS spectrum is composed of the Cr $2p_{3/2}$ and Cr $2p_{1/2}$ peaks. Both peaks have two components, indicating the presence of two valences. While the component with lower binding energy can be assigned to Cr^{3+}, the higher binding energy (located at 581 eV for $2p_{3/2}$ and 592 eV for $2p_{1/2}$) is characteristic for Cr^{6+}. The Cr^{6+} component is derived from the surface since its intensity decreases with X-ray energy *E*. Assuming that photoelectron escape depth is 2 nm for $E = 1253.6$ eV and 8 nm for $E = 7953$ eV, the thickness of the surface Cr^{6+} layer is estimated to be 1.06 and 1.10 nm from the intensity ratio between the surface Cr^{6+} and bulk Cr^{3+} components obtained at $E = 1253.6$ eV and $E = 7953$ eV, respectively. These values are consistent with one another and agree with that observed by HRTEM. It should be noted that formation of a surface layer with a d^0 ion was found for $MgTi_2O_4$ as well,[43] and that a Cr^{6+} contribution is present even in our XPS specra for $SrCrO_3$ measured as a reference. Here, one can safely conclude that the Cr^{6+} is derived from the surface amorphous $PbCr^{6+}O_4$ layer observed by our HRTEM study. The charge-transfer satellite is clearly observed in $PbCrO_3$ which is similar to $LaCr^{3+}O_3$[32] and is different from $SrCr^{4+}O_3$. The binidng energy and the charge-transfer satellite of the bulk component are consistent with $La^{3+}Cr^{3+}O_3$, and the charge-transfer satellite is well reproduced by the cluster model calculation for Cr^{3+} oxides[32] after the subtraction of the Cr^{6+} contribution from the amorphous $PbCrO_4$. Both of the above results clearly show that the bulk Cr valence is 3+. We suspect that the Cr^{6+} component found in the XAS data[26] is coming from the surface of the particles.

Our first-principles calculations also confirm that the valence of Cr should be 3+, accompanied by a charge disproportionation at Pb site. Namely, we searched for the ground-state structure of $PbCrO_3$ in a systematic way, by examining all possible combinations of Jahn−Teller and tilting modes.[44] Carpenter and Howard showed that these combinations allow for 44 different crystal symmetries.[45] In addition to Jahn−Teller and tilting modes, we incorporated all modes that are allowed by symmetry of the particular space group at the Wyckoff positions of Pb, Cr, and O and carried out a full structural relaxation for each of the 44 possible symmetries, the largest simulation cell containing 8 formula units of $PbCrO_3$. We do cover the full set of tilt structures that lead to different patterns of cation charges. In particular, we find that the lowest-energy structure is characterized by a 3+ charge on Cr and a 2+/4+ charge-ordered Pb sublattice. We present the density of states of the relevant atomic orbitals for the calculated ground-state structure in Figure 2D, where it can be seen that the charge order leads to insulating behavior (we include the corresponding band structure in the inset of the same figure where the band gap is more obvious). The ground state we find is centrosymmetric, characterized by the *Pmnm* (No. 59) symmetry and tilts of oxygen octahedra (see Table S4 and Figure 2E). The distance between the apical oxygens of the CrO_6 octahedra is ∼4 Å, in good agreement with experiment. However, due to the tilts of the octahedra, the calculated pseudocubic lattice parameter is ∼3.4% smaller than the experimentally measured one. Additionaly, we employed a

DOI: 10.1021/jacs.5b08216
J. Am. Chem. Soc. 2015, 137, 12719−12728

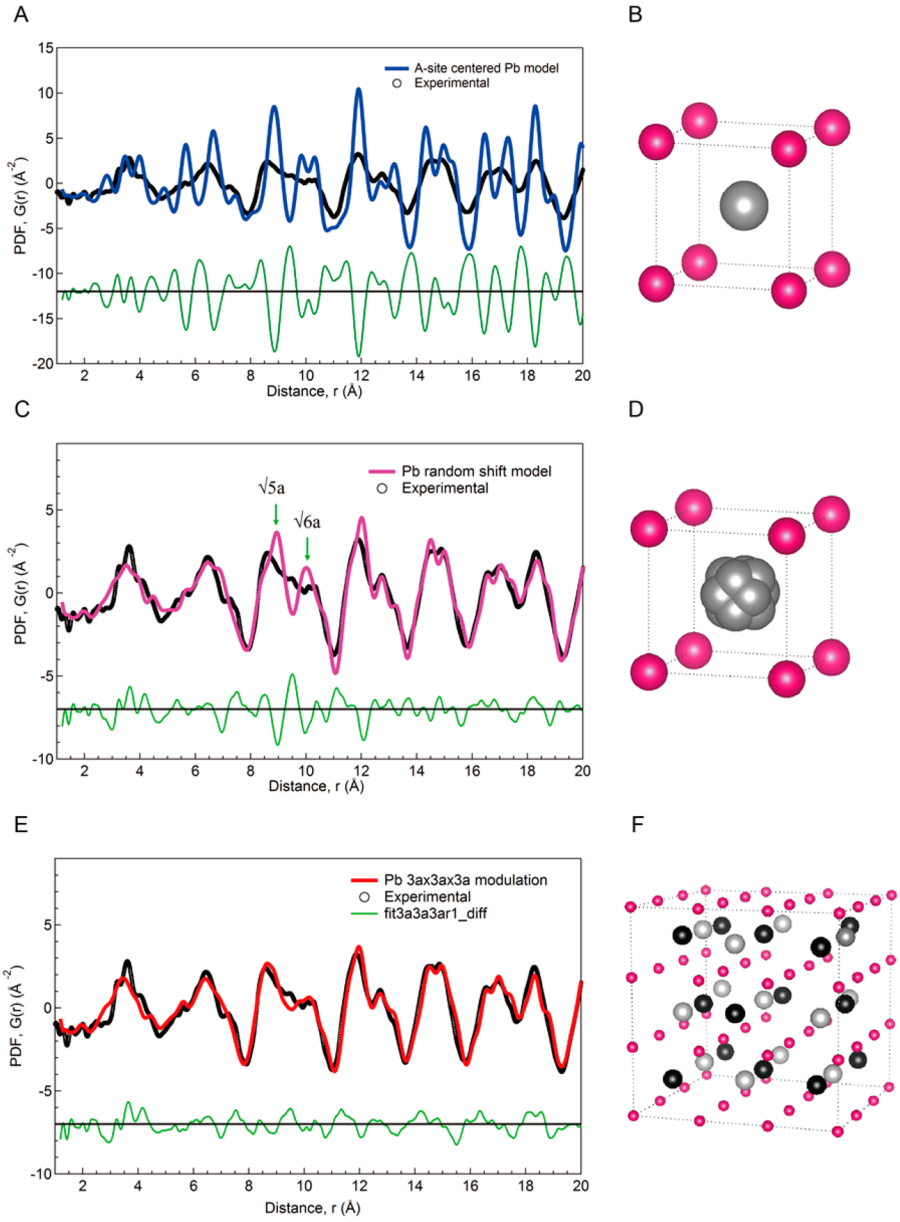

Figure 3. PDF data for $PbCrO_3$ revealing the presence of short-range Pb−Pb correlation. (A) Observed (open circles) and calculated (blue line) PDF of an A-site centered Pb model. (B) Crystal structure of $PbCrO_3$ with an A-site centered Pb model. (C) Observed (open circles) and calculated (pink line) PDF of a random Pb-shift model (pink line). The Pb position is split in 12 equiv 110 directions with the refined shift by fitting of 0.44 Å. (D) Crystal structure of $PbCrO_3$ with a random Pb-shift model. (E) Observed (open circles) and calculated (red line) PDF of an ordered model with $3a_0 \times 3a_0 \times 3a_0$ superstructure. (F) The refined crystal structure of the ordered model with $3a_0 \times 3a_0 \times 3a_0$ superstructure. In all of the crystal structures the pink color atoms are Cr and the other atoms are Pb. Oxygen atoms are not shown. In all the models the isotropic displacement parameters of each element are fixed at U_{iso}(Pb) = 0.02 Å^2, U_{iso}(Cr) = 0.01 Å^2, and U_{iso}(O) = 0.02 Å^2.

genetic algorithm to investigate possible structures in a 40-atom unit cell with variable lattice vectors and found that most of the low-energy perovskite structures are localized in the vicinity of our previously determined ground-state orthorhombic structure (having similar volumes too). Analyzing these low-energy structures, we found that there is some degree of freedom in positions of Pb atoms, accompanied by various tilting patterns of oxygen octahedra, which leads to many metastable states in a very narrow range of energies (about 0.15 eV/f.u.) depicted by the black circles in Figure 2F. This result may suggest the degeneracy of the ground state, in other words, the ground state may in fact be structurally frustrated, leading to the increased volume and a glassy charge distribution on the Pb site. In this sense, the charge ordered state we present in Figure 2D and 2E is merely a representative of a group of the lowest energy states. Notably, in a fully symmetric cubic perovskite unit cell, without the tilts and Pb displacements, no charge order and no band gap is observed in the calculations. We performed an additional check by comparing the total energies of our ground state with the (insulating) state characterized by the Cr−Pb antisite defects, suggested in ref 25: the charge-ordered ground state we found lies 0.30 eV/f.u. lower in energy. The simple cubic perovskite structure of $Pb^{2+}Cr^{4+}O_3$ is 0.38 eV/f.u. higher than the *Pmnm* one. We note that we have also performed a genetic-algorithm based scan of the possible states in a $3a_0 \times 3a_0 \times 3a_0$ supercell suggested by the diffuse

DOI: 10.1021/jacs.5b08216
J. Am. Chem. Soc. 2015, 137, 12719−12728

scatterings observed in our diffraction data. While here the charge order on Pb sites is suppressed (due to the odd number of Pb atoms), we found a state with a volume close to the experimental one, with charge disproportionated Cr site, as suggested in ref 26. In order to compare this possibility to the scenario in which a charge disproportionation on Pb site takes place and allow for the antiferromagnetic ordering of Cr, we enlarged the unit cell found by the genetic algorithm to the one containing 54 formula units and relaxed the atomic positions and the cell volume again. This resulted in an insulating antiferromagnetic state with $8Cr^{6+}$, $12Cr^{5+}$, $6Cr^{4+}$ and $28Cr^{3+}$. However, the energy of this Cr-charge-disproportionated state (large green circle in Figure 2F) is very close to that of the simple cubic high-pressure phase, similar to the phase suggested in ref 26. This places it approximately 0.3 eV/f.u. higher than the Pb-charge-disproportionated model we propose. We note that our Pb-charge-ordered state continues to be the ground state also for smaller values of the Hubbard U: for U = 3 eV and J = 1 eV, we find that this state is approximately 120 meV lower than the Cr-disproportionated one, and 160 meV lower than the simple cubic state. If we lower the Hubbard U further, to U = 2 eV and J = 1 eV, both charge-disproportionated states collapse to the metallic cubic phase. For further comparison with previously published ab initio studies, we include in Figure 2F our calculation of a metallic tetragonal state with $P4mm$ symmetry as suggested by Ganesh and Cohen[24] (indicated by the orange square) and note that, although we also find it to be a local energy minimum, we could not reproduce the high volume of this state reported in ref 24. Finally, we note that our model with all Cr atoms in a formal charge state of 3+ fits well the observed picture of the superexchange driven simple G-type antiferromagnetic ordering. The alternative possibilities involving various Cr-charge disproportionation patterns and/or Jahn−Teller type distortions and orbital ordering (that could lead to insulating behavior in case Cr was in oxidation state 4+) could possibly yield more complicated magnetization patterns than experimentally observed G-type ordering.

Although the complete long-range ordering of Pb^{2+} and Pb^{4+} that yields the lowest-energy structure in our calculation was not found in the structural studies, modulated local structure was suggested by TEM observation. PDF analysis of synchrotron X-ray total scattering data was performed to investigate the local structure. We first assumed a cubic unit cell with Pb at the body center (see Figure 3B). The agreement of the calculated and observed PDF data was quite poor as shown in Figure 3A. Then the Pb position was split in 12 equiv 110 directions (see Figure 3D) with the refined shift of 0.44 Å. For both models, isotropic thermal displacement parameters for Pb and Cr were fixed to rather large values, U_{iso}(Pb) = 0.02 Å^2, U_{iso}(Cr) = 0.01 Å^2 and U_{iso}(O) = 0.02 Å^2. The split of Pb positions drastically improved the fitting (Figure 3C) in the higher r region (r > ∼12 Å). On the other hand, the peak shape in the lower r region (r < ∼12 Å) is still not well reproduced. The discrepancy in the lower r region, most significant for peaks at $\sqrt{6}a_0$ and $\sqrt{5}a_0$ indicates that the Pb shift is not random (see Figure 3C), but short-range correlation to each other is present. The correlation length of Pb displacement is 12 Å, approximately $3a_0$, is consistent with the periodicity of modulation estimated from the location of diffuse intensity in the FFT image. Next we employed an ordered model with $3a_0 \times 3a_0 \times 3a_0$ superstructure. The 27 Pb sites are divided into 2 groups, A and B, corresponding to Pb^{2+} and Pb^{4+} or vice versa as clarified by HAXPES with the rock-salt type arrangement as shown in Figure 3F. Then, longitudinal wave type shift of the Pb positions were applied to both sublatttices. The Pb positions were constrained so that these form sine waves in a, b, and c directions. Namely, the Pb coordinates of $3a_0 \times 3a_0 \times 3a_0$ cell were expressed by the following formula

$$(x, y, z)^i = \{a_x^i \sin(2\pi x_0^i + \varphi_x^i) + x_0^i,\ a_y^i \sin(2\pi y_0^i + \varphi_y^i) + y_0^i,\ a_z^i \sin(2\pi z_0^i + \varphi_z^i) + z_0^i\}$$

where $i = A$ or B for sublattice A or B respectively, and (x_0, y_0, z_0) is the coordinates of A-cite center. Positions of Cr and O were fixed to the corners of each 27 cube and at the centers of two Cr ions, respectively. The fitting further improved as shown in Figure 3E, especially the discrepancy of the intensities of peaks at $\sqrt{6}a_0$ and $\sqrt{5}a_0$ is solved. The amplitudes and the phases of the sine waves were refined to

$$(a_x^A, a_y^A, a_z^A, \varphi_x^A, \varphi_y^A, \varphi_z^A) = \{0.048(1), 0.002(1), 0.058(1), 1.51(2), 1.4(5), 1.18(2)\}$$

$$(a_x^B, a_y^B, a_z^B, \varphi_x^B, \varphi_y^B, \varphi_z^B) = \{0.014(4), 0.021(3), -0.036(3), 0.6(2), 1.2(1), 1.05(7)\}$$

The crystal structure parameters derived from these values are found in Table S5. The averaged displacements of Pb positions of sublattice A and B are 0.66 and 0.36 Å, respectively. These large displacements are the origin of relatively large U_{iso}(Pb) and are the most probably caused by the stereo active $6s^2$ lone pairs of Pb^{2+}. Similar distorted $Bi^{3+}O_6$ octahedron was found in $BiNiO_3$.[8] The coexistence of large Pb^{2+} and small Pb^{4+} further enhances the displacements. The difference between the values of the two sublattices is attributed to the difference of the valence of Pb ions. It should be noted that the distribution in the Pb−Pb lengths, 3.4−4.2 Å agrees quite well with that estimated from the HAADF image (3.5−4.3 Å). To achieve further agreement in lower r region, oxygen positions should also be shifted. Unfortunately we cannot prepare a large amount of the high-quality sample required for neutron PDF study as discussed below. Other models, rock-salt ordering with transverse wave type shifts, columnar type and layered type orderings of Pb^{2+} and Pb^{4+} and simple application of transverse or longitudinal wave type shift of Pb positions without the ordering of Pb^{2+} and Pb^{4+} sites were also examined, but the best fit was obtained for the rock-salt ordering model with longitudinal wave type Pb position shifts. It should be noted that the numbers of Pb^{2+} and Pb^{4+} are different in the $3a_0 \times 3a_0 \times 3a_0$ cell, 14:13 or vice versa. Furthermore, there are A−A or B−B arrangements at the interface between $3a_0 \times 3a_0 \times 3a_0$ cells. The long-range ordering of Pb^{2+} and Pb^{4+} is therefore prohibited, resulting in the absence of super lattice spots in ED, but the presence of diffuse scattering instead. Because of the absence of superlattice peaks, the PDF analysis was very useful for investigating the distorted structure. Simulation of HRTEM image or Rietveld analysis of SXRD data were impossible. Taking into account the result of PDF, the short-range correlation of the Pb positions, one can conclude that Pb^{2+} and Pb^{4+} form a glassy structure, namely, charge glass.

DOI: 10.1021/jacs.5b08216
J. Am. Chem. Soc. 2015, 137, 12719−12728

Our PDF analysis indicates the modulation of Pb positions from the centers of Cr cubes. On the other hand, Pb atoms in our calculated model are confined in narrow tunnels formed by buckled Cr−O−Cr bonds (in other words, tilted CrO_6 octahedra) which makes the volume smaller than the experimental value. We conjecture that the structural frustration blocks the coherent tilting of the octahedra and leads to the observed modulation of Pb positions and a larger volume. Note that A-site cation dynamics could also block the oxygen-octahedra tilts, as suggested in case of $EuTiO_3$.[47] Since our calculated volume is underestimated, the EOS curve of $Pb^{2+}_{0.5}Pb^{4+}_{0.5}Cr^{3+}O_3$ phase in Figure 2F should be shifted to the large volume side, and should cross with that for the simple cubic and metallic $Pb^{2+}Cr^{4+}O_3$ phase. This assumption could explain the experimentaly observed pressure induced volume collapse and also predicts an insulator to metal transition.

The valence state of $PbCrO_3$ is thus determined to be $Pb^{2+}_{0.5}Pb^{4+}_{0.5}Cr^{3+}O_3$. The insulating nature of $PbCrO_3$ reflects the Cr^{3+} electronic configuration with half-filled t_{2g} orbitals as that in $LaCrO_3$.[48] The remaining problem is the ordered magnetic moment of 2 μ_B, rather than 3 μ_B expected for Cr^{3+} determined by neutron diffraction. We performed the analysis of neutron diffraction data collected on our sample shown in Figure S2. Even assuming the splitting of the Pb position as suggested by the PDF data, the determined Cr magnetic moment was still 2.10(6) μ_B. This may be a consequence of the magnetically frustrated nature of the lattice leading to incomplete magnetic ordering or a reflection of the itinerint nature of the Cr ion. It is possible that the ordered moment of $PbCrO_3$ is smaller than that expected for Cr^{3+} owing to the presence of antiferromagnetic second nearest neighbor interaction. A peak at around 39 deg, which appears at low temperatures, is suggestive of noncollinear spin structure. Although our polarized neutron scattering data shown in Figure S3 revealed that it was magnetic in origin, the transition temperature was considerably higher than that of $PbCrO_3$. The peak should be attributed to the secondary phase, probably 0 3/2 1/2 or 1 3/2 0 peak of Pb_2CrO_5.[49] The simple G-type spin structure is thus confirmed.

Pressure effects on the structure and electrical resistivity of $PbCrO_3$ were investigated next. Pressure dependence of energy-dispersive SXRD patterns is shown in Figure 4A. A sudden shift of peak positions to the high-energy side, indicating shrinkage of the lattice, is observed for pressures between 2 and 3 GPa. The lattice parameters calculated from the peak positions are plotted in Figure 4B as a function of pressure. The lattice parameters' decrease by 2.7%, corresponding to a volume collapse of 7.8% at 2.5 GPa, as previously reported, is confirmed for the present sample as well. The electrical resistivity shown in Figure 4C suddenly drops at the corresponding pressure and the temperatue dependence shown in the inset clearly indicates the insulator to metal transition at this pressure. As stated above, it was clarified that the valence state of $PbCrO_3$ was $Pb^{2+}_{0.5}Pb^{4+}_{0.5}Cr^{3+}O_3$ under ambient conditions. The observed volume collapse and simultaneous insulator-to-metal transition can be explained by assuming a pressure-induced intermetallic charge transfer between Pb^{4+} and Cr^{3+} ions and a $Pb^{2+}Cr^{4+}O_3$ valence state for the high-pressure phase. Indeed, the lattice parameter of the high-pressure phase is close to that of $SrCrO_3$, which has a $Sr^{2+}Cr^{4+}O_3$ valence state. Such a charge-transfer transition accompanied by an insulator-to-metal transition and volume decrease was established for $BiNiO_3$[9,10,50] and $LaCu_3Fe_4O_{12}$.[13]

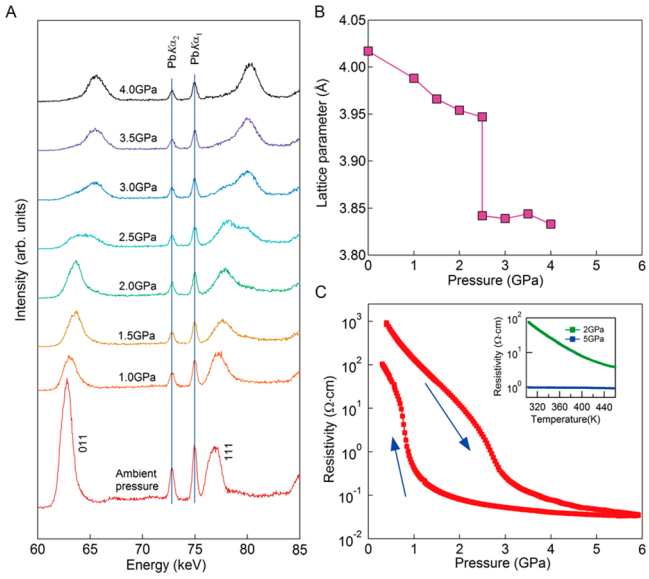

Figure 4. Pressure effect on $PbCrO_3$ indicating the $Pb^{2+}_{0.5}Pb^{4+}_{0.5}Cr^{3+}O_3$ to $Pb^{2+}Cr^{4+}O_3$ intermetallic charge transfer transition. (a) Energy-dispersive SXRD patterns at high pressure. Characteristic X-rays from lead are indicated with vertical lines. (b) Lattice parameter as a function of pressure. The error bars for the lattice parameter are smaller than the corresponding symbols. (c) Pressure dependence of electrical resistivity of $PbCrO_3$ at room temperature. Inset shows the temperature dependence of electrical resistivity under 2 and 5 GPa.

In all of these cases, Pb(Bi) disproportionation is induced by the instability of $Pb^{3+}(Bi^{4+})$ with $6s^1$ electronic configurations.[5]

The insulator to metal transition and volume collapse due to the Pb−Cr charge transfer observed for $PbCrO_3$ is induced not only by application of pressure, but also by Sr substitution for Pb. Figure 5A shows the SXRD patterns for $Pb_{1-x}Sr_xCrO_3$. All the peaks shift to the high-angle side between x = 0.1 and 0.6, indicating a shrinkage of the lattice. Two phases coexist for x = 0.2 to 0.5. The lattice constants plotted in Figure 5B clearly show that $Pb_{1-x}Sr_xCrO_3$ can be divided into $PbCrO_3$- and $SrCrO_3$-type phases with 11% volume difference. The electrical resistivity at 300 K is also plotted in the same figure. The insulator-to-metal transition reflects the Cr^{3+} to Cr^{4+} valence change and the decrease of the FWHM of the SXRD peak from 0.049 deg. for the lead-rich phase to 0.030 deg. for the strontium-rich phase (see Figure 5A) due to the disappearance of Pb^{2+}+Pb^{4+} disproportionation. Our O-K edge XAS data shown in Figure S4 support this scenario.

4. CONCLUSION

In conclusion the valence state of $PbCrO_3$ was investigated using a newly synthesized phase pure sample. PDF analysis of the synchrotron X-ray scattering and XPS data clearly indicated a $Pb^{2+}_{0.5}Pb^{4+}_{0.5}Cr^{3+}O_3$ valence state with local ordering of Pb^{2+} and Pb^{4+}, which can be termed charge glass. The partial ordering of Pb^{2+} and Pb^{4+} was found to be the origin of the modulated structure observed by HRTEM, while Cr^{3+} gives the insulating nature and a large lattice parameter compared with that of $SrCrO_3$. DFT calculations confirm a Pb^{2+}/Pb^{4+} charge-ordered ground state. The origin of the glassy nature of Pb^{2+}/Pb^{4+} distribution is not clear at this stage. We examined the possibility of deviation of the Pb^{2+}/Pb^{4+} ratio from 1:1 because of the partial charge transfer between Pb and Cr, but judging

DOI: 10.1021/jacs.5b08216
J. Am. Chem. Soc. 2015, 137, 12719−12728

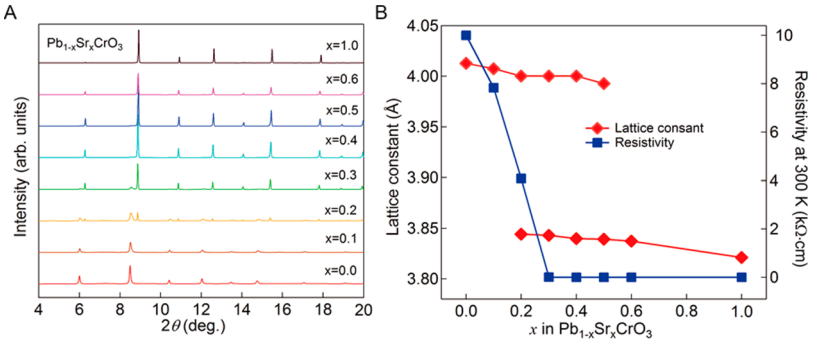

Figure 5. Doping effect on $Pb_{1-x}Sr_xCrO_3$. (A) SXRD pattern of $Pb_{1-x}Sr_xCrO_3$. (B) Lattice parameter and resistivity at 300 K of $Pb_{1-x}Sr_xCrO_3$ as functions of strontium content x. The error bars for the lattice parameter and resistivity are smaller than the corresponding symbols.

from the highly insulating character, the deviation of Cr valence from 3+ is less than 5%.[51] The glassy state may be common for the "valence skipper" elements. Indeed, possible $Pb^{2+}{}_{0.5}Pb^{4+}{}_{0.5}FeO_3$[52] valence state and the absence of Bi^{3+}/Bi^{5+} ordering in $(Bi_{0.8}Pb_{0.2})^{4+}Ni^{2+}O_3$[53] perovskite were reported by the authors. These are the next candidates for the observation of Pb^{2+}/Pb^{4+} or Bi^{3+}/Bi^{5+} glass state. A pressure-induced intermetallic charge transfer between Pb^{4+} and Cr^{3+} leads to a metallic $Pb^{2+}Cr^{4+}O_3$ high-pressure phase. The large volume collapse was attributed to the oxidation of chromium ions from Cr^{3+} to Cr^{4+}. A similar insulator-to-metal transition accompanied by the volume decrease was also induced by strontium substitution for lead. Since the insulator to metal transition is due to the valence change of Cr ion, rather than the melting of Pb charge glass, we can not investigate the glassy nature by the transport measurements. Thermodynamical studies under pressure are desired. We note that the valence distributiuon of Pb-3d transition metal perovskte systematically changes from $Pb^{2+}Ti^{4+}O_3$ and $Pb^{2+}V^{4+}O_3$[54] to $Pb^{2+}{}_{0.5}Pb^{4+}{}_{0.5}Cr^{3+}O_3$ and finally to $Pb^{4+}Ni^{2+}O_3$[55] as the d-level of the transition metal becomes deeper. The experimental and theoretical investigation of such composition dependent intermetallic charge transfer should be a big challenge.

■ ASSOCIATED CONTENT

Supporting Information

The Supporting Information is available free of charge on the ACS Publications website at DOI: 10.1021/jacs.5b08216.

HAXPES spectrum of $BiNiO_3$, Rietveld refinement of the neutron powder diffraction data on $PbCrO_3$ at 4 K, temperature dependence of the magnetic intensities of $PbCrO_3$ 111 peak and the unknown peak at 39 deg., measured using polarized neutron diffraction technique, O-*K* edge XAS data for $Pb_{1-x}Sr_xCrO_3$, Rietveld refinement result of $PbCrO_3$ at room temperature, fitting results for Pb-4f core level of XPS on pure $PbCrO_3$ and Bi-4f core level of XPS on pure $BiNiO_3$, theoretical structural parameters of $PbCrO_3$ and refined crystal structure parameters of $PbCrO_3$ with ordered model of $3a_0 \times 3a_0 \times 3a_0$ superstructure. (PDF)

■ AUTHOR INFORMATION

Corresponding Authors

*yu.r.aa@m.titech.ac.jp
*mazuma@msl.titech.ac.jp

Present Addresses

■Center for High Pressure Science & Technology Advanced Research, 1690 Cailun Rd, Bldg 6, Pudong, Shanghai, 201203, PR China.
○Department of Applied Physics, Waseda University, 3-4-1 Okubo, Shinjuku-ku, Tokyo 169−8555, Japan.
▲Department of Applied Chemistry, Faculty of Science and Engineering, Chuo University, 1-13-27 Kasuga, Bunkyo-ku, Tokyo 112−8551, Japan.
●Department of Computer Science, University of California Davis, Davis, California 95616, United States.
△Max Planck Institute for Solid State Research, Heisenbergstrasse 1, Stuttgart 70569, Germany.

Notes

The authors declare no competing financial interest.

■ ACKNOWLEDGMENTS

We thank Dr. Shigenori Ueda of Synchrotron X-ray Station at SPring-8, and Synchrotron X-ray Group, Quantum Beam Unit, National Institute for Materials Science (NIMS) for his help in HAXPES measurement. This work was partially supported by the Cabinet Office, Government of Japan through its "Funding Program for Next-Generation World-Leading Researchers" (GR032), Grant-in-Aid for Scientific Research on Innovative Areas (26106507), Young Scientists (B) (26820291, and 26800180) and 15K14119 from the Japan Society for the Promotion of Science (JSPS), Kanagawa Academy of Science and Technology and by the Young Investigators Group Program of the Helmholtz Association ("Computational Nanoferronics Laboratory", VH-NG-409), Germany. The synchrotron-radiation experiments were performed at SPring-8 with the approval of the Japan Synchrotron Radiation Research Institute (2012A1008, 2012A3612, 2012A3701, 2012B1787, 2013A3615, 2013A3703, 2014A4905) and under the Shared User Program of JAEA Facilities (2012A-E18 and 2013A-E16) with the approval of Nanotechnology Platform project supported by the Ministry of Education, Culture, Sports, Science and Technology (A-13-AE-0011). Research conducted at ORNL's High Flux Isotope Reactor was sponsored by the Scientific User Facilities Division, Office of Basic Energy Sciences, US Department of Energy. First-principles calculations were supported by the Jülich Supercomputing Centre (project JIFF38) and JARA-HPC from RWTH Aachen University under Project jara0081.

DOI: 10.1021/jacs.5b08216
J. Am. Chem. Soc. 2015, 137, 12719−12728

REFERENCES

(1) Mori, S.; Katsufuji, T.; Yamamoto, N.; Chen, C. H.; Cheong, S. W. *Phys. Rev. B: Condens. Matter Mater. Phys.* **1999**, *59*, 13573.
(2) Takano, M.; Nakanishi, N.; Takeda, Y.; Naka, S.; Takada, T. *Mater. Res. Bull.* **1977**, *12*, 923.
(3) Dagotto, E. *Science* **2005**, *309*, 257.
(4) Kagawa, F.; Sato, T.; Miyagawa, K.; Kanoda, K.; Tokura, Y.; Kobayashi, K.; Kumai, R.; Murakami, Y. *Nat. Phys.* **2013**, *9*, 419.
(5) Harrison, W. A. *Phys. Rev. B: Condens. Matter Mater. Phys.* **2006**, *74*, 245128.
(6) Bode, H. *Lead-Acid Batteries*; John Wiley and Sons, Inc.: New York, 1977.
(7) Cox, D. E.; Sleight, A. W. *Acta Crystallogr., Sect. B: Struct. Crystallogr. Cryst. Chem.* **1979**, *35*, 1.
(8) Ishiwata, S.; Azuma, M.; Takano, M.; Nishibori, E.; Takata, M.; Sakata, M.; Kato, K. *J. Mater. Chem.* **2002**, *12*, 3733.
(9) Azuma, M.; Carlsson, S.; Rodgers, J.; Tucker, M. G.; Tsujimoto, M.; Ishiwata, S.; Isoda, S.; Shimakawa, Y.; Takano, M.; Attfield, J. P. *J. Am. Chem. Soc.* **2007**, *129*, 14433.
(10) Azuma, M.; Chen, W. T.; Seki, H.; Czapski, M.; Olga, S.; Oka, K.; Mizumaki, M.; Watanuki, T.; Ishimatsu, N.; Kawamura, N.; Ishiwata, S.; Tucker, M. G.; Shimakawa, Y.; Attfield, J. P. *Nat. Commun.* **2012**, *2*, 347.
(11) Seda, T.; Hearne, G. R. *J. Phys.: Condens. Matter* **2004**, *16*, 2707.
(12) Huang, Z. X.; Auckett, J. E.; Blanchard, P. E. R.; Kennedy, B. J.; Miiller, W.; Zhou, Q. D.; Avdeev, M.; Johnson, M. R.; Zbiri, M.; Garbarino, G.; Marshall, W. G.; Gu, Q. F.; Ling, C. D. *Angew. Chem., Int. Ed.* **2014**, *53*, 3414.
(13) Long, Y. W.; Hayashi, N.; Saito, T.; Azuma, M.; Muranaka, S.; Shimakawa, Y. *Nature* **2009**, *458*, 60.
(14) Roth, W. L.; DeVries, R. C. *J. Appl. Phys.* **1967**, *38*, 951.
(15) Chamberland, B. L.; Moeller, C. W. *J. Solid State Chem.* **1972**, *5*, 39.
(16) DeVries, R. C.; Roth, W. L. *J. Am. Ceram. Soc.* **1968**, *51*, 72.
(17) Zhou, J. S.; Jin, C. Q.; Long, Y. W.; Yang, L. X.; Goodenough, J. B. *Phys. Rev. Lett.* **2006**, *96*, 046408.
(18) Komarek, A. C.; Möller, T.; Isobe, M.; Drees, Y.; Ulbrich, H.; Azuma, M.; Fernández-Díaz, M. T.; Senyshyn, A.; Hoelzel, M.; André, G.; Ueda, Y.; Grüninger, M.; Braden, M. *Phys. Rev. B: Condens. Matter Mater. Phys.* **2011**, *84*, 125114.
(19) Komarek, A. C.; Streltsov, S. V.; Isobe, M.; Möller, T.; Hoelzel, M.; Senyshyn, A.; Trots, D.; Fernández-Díaz, M. T.; Hansen, T.; Gotou, H.; Yagi, T.; Ueda, Y.; Anisimov, V. I.; Grüninger, M.; Khomskii, D. I.; Braden, M. *Phys. Rev. Lett.* **2008**, *101*, 167204.
(20) Ortega-San-Martin, L.; Williams, A. J.; Rodgers, J.; Attfield, J. P.; Heymann, G.; Huppertz, H. *Phys. Rev. Lett.* **2007**, *99*, 255701.
(21) Arévalo-López, A. M.; Dos santos-García, A. J.; Alario-Franco, M. A. *Inorg. Chem.* **2009**, *48*, 5434.
(22) Xiao, W. S.; Tan, D. Y.; Xiong, X. L.; Liu, J.; Xu, J. *Proc. Natl. Acad. Sci. U. S. A.* **2010**, *107*, 14026.
(23) Wang, W. D.; He, D. W.; Xiao, W. S.; Wang, S. M.; Xu, J. A. *Chin. Phys. Lett.* **2013**, *30*, 117201.
(24) Ganesh, P.; Cohen, R. E. *Phys. Rev. B: Condens. Matter Mater. Phys.* **2011**, *83*, 172102.
(25) Wang, B. T.; Yin, W.; Li, W. D.; Wang, F. W. *J. Appl. Phys.* **2012**, *111*, 013503.
(26) Cheng, J. G.; Kweon, K. E.; Larregola, S. A.; Ding, Y.; Shirako, Y.; Marshall, L. G.; Li, Z. Y.; Li, X.; dos Santosg, A. M.; Suchomel, M. R.; Matsubayashi, K.; Uwatoko, Y.; Hwang, G. S.; Goodenough, J. B.; Zhou, J. S. *Proc. Natl. Acad. Sci. U. S. A.* **2015**, *112*, 1670.
(27) Arévalo-López, A. M.; Alario-Franco, M. A. *J. Solid State Chem.* **2007**, *180*, 3271.
(28) Watanuki, T.; Machida, A.; Ikeda, T.; Ohmura, A.; Kaneko, H.; Aoki, K.; Sato, T. J.; Tsai, A. P. *Philos. Mag.* **2007**, *87*, 2905.
(29) Egami, T.; Billinge, S. J. L. *Underneath the Bragg Peaks: Structural Analysis of Complex Materials*; Pergamon, Oxford, U.K., 2003.
(30) Qiu, X.; Thompson, J. W.; Billinge, S. J. L. *J. Appl. Crystallogr.* **2004**, *37*, 678.
(31) Farrow, C. L.; Juhas, P.; Liu, J. W.; Bryndin, D.; Božin, E. S.; Bloch, J.; Proffen, T.; Billinge, S. J. L. *J. Phys.: Condens. Matter* **2007**, *19*, 335219.
(32) Saitoh, T.; Bouquet, A. E.; Mizokawa, T.; Fujimori, A. *Phys. Rev. B: Condens. Matter Mater. Phys.* **1995**, *52*, 7934.
(33) Perdew, J. P.; Burke, K.; Ernzerhof, M. *Phys. Rev. Lett.* **1996**, *77*, 3865.
(34) Perdew, J. P.; Ruzsinszky, A.; Csonka, G. I.; Vydrov, O. A.; Scuseria, G. E.; Constantin, L. A.; Zhou, X. L.; Burke, K. *Phys. Rev. Lett.* **2008**, *100*, 136406.
(35) Lichtenstein, A. I.; Asinimov, V. I.; Zaanen, J. *Phys. Rev. B: Condens. Matter Mater. Phys.* **1995**, *52*, 5467.
(36) Kresse, G.; Furthmüller, J. *Phys. Rev. B: Condens. Matter Mater. Phys.* **1996**, *54*, 11169.
(37) Blöchl, P. E. *Phys. Rev. B: Condens. Matter Mater. Phys.* **1994**, *50*, 17953.
(38) Oganov, A. R.; Glass, C. W. *J. Chem. Phys.* **2006**, *124*, 244704.
(39) Oganov, A. R.; Stokes, H.; Valle, M. *Acc. Chem. Res.* **2011**, *44*, 227.
(40) Lyakhov, A. O.; Oganov, A. R.; Stokes, H.; Zhu, Q. *Comput. Phys. Commun.* **2013**, *184*, 1172.
(41) Vickerman, J. C.; Gilmore, I. *Surface Analysis: The Principal Techniques*, 2nd ed.; Wiley: New York, 2009.
(42) Brown, I. D.; Altermatt, D. *Acta Crystallogr., Sect. B: Struct. Sci.* **1985**, *41*, 244 (r_0 = 1.708, B = 0.37).
(43) Fujiwara, H.; Ishige, Y.; Mizokawa, T.; Sasaki, T.; Isobe, M.; Ueda, Y. *APL Mater.* **2013**, *1*, 022110.
(44) Schlipf, M. Heyd-Scuseria-Ernzerhof Screened-Exchange Hybrid Functional for Complex Materials: All-Electron Implementation and Application, Ph.D. Thesis, University in Aachen, Germany, 2012.
(45) Carpenter, M. A.; Howard, C. J. *Acta Crystallogr., Sect. B: Struct. Sci.* **2009**, *65*, 134.
(46) Murnaghan, F. D. *Proc. Natl. Acad. Sci. U. S. A.* **1944**, *30*, 244.
(47) Bessas, D.; Rushchanskii, K. Z.; Kachlik, M.; Disch, S.; Gourdon, O.; Bednarcik, J.; Maca, K.; Sergueev, I.; Kamba, S.; Ležaić, M.; Hermann, R. P. *Phys. Rev. B: Condens. Matter Mater. Phys.* **2013**, *88*, 144308.
(48) Imada, M.; Fujimori, A.; Tokura, Y. *Rev. Mod. Phys.* **1998**, *70*, 1039.
(49) Indovski, B.; Singh, M. P.; Razavi, F. S. *J. Magn. Magn. Mater.* **2013**, *331*, 72.
(50) Ishiwata, S.; Azuma, M.; Hanawa, M.; Moritomo, Y.; Ohishi, Y.; Kato, K.; Takata, M.; Nishibori, E.; Sakata, M.; Terasaki, I.; Takano, M. *Phys. Rev. B: Condens. Matter Mater. Phys.* **2005**, *72*, 045104.
(51) Pal, S.; Heberta, S.; Yaicle, C.; Martin, C.; Maignan, A. *Eur. Phys. J. B* **2006**, *53*, 5.
(52) Tsuchiya, T.; Saito, H.; Yoshida, M.; Katsumata, T.; Ohba, T.; Inaguma, Y.; Takao Tsurui, T.; Shikano, M. *Mater. Res. Soc. Symp. Proc.* **2006**, *988*, QQ09−16.
(53) Ishiwata, S.; Azuma, M.; Takano, M. *Chem. Mater.* **2007**, *19*, 1964.
(54) Belik, A. A.; Azuma, M.; Saito, T.; Shimakawa, Y.; Takano, M. *Chem. Mater.* **2005**, *17*, 269.
(55) Inaguma, Y.; Tanaka, K.; Tsuchiya, T.; Mori, D.; Katsumata, T.; Ohba, T.; Hiraki, K.; Takahashi, T.; Saitoh, H. *J. Am. Chem. Soc.* **2011**, *133*, 16920.

DOI: 10.1021/jacs.5b08216
J. Am. Chem. Soc. 2015, 137, 12719−12728